

RESEARCH ARTICLE | AUGUST 08 2024

Field emission control by work function modulation in graphene edge cathodes ^{EP}

Cheul Hyun Yoon ^{ID} ; Gyeong Min Seo ^{ID} ; Seok Hyun Yoon ^{ID} ; Byoung Don Kong [✉] ^{ID}*J. Appl. Phys.* 136, 064501 (2024)<https://doi.org/10.1063/5.0215449>

Articles You May Be Interested In

Synergistic regulation of device performance by structural parameters of vertical side-gate type vacuum channel field emission transistor

J. Vac. Sci. Technol. B (March 2025)

A model of carrier density and drain current for monolayer graphene field-effect transistors

AIP Advances (February 2019)

Piezoelectric graphene field effect transistor pressure sensors for tactile sensing

Appl. Phys. Lett. (July 2018)



Nanotechnology & Materials Science



Optics & Photonics



Impedance Analysis



Scanning Probe Microscopy



Sensors



Failure Analysis & Semiconductors



Unlock the Full Spectrum. From DC to 8.5 GHz.

Your Application. Measured.

[Find out more](#)

Field emission control by work function modulation in graphene edge cathodes



Cite as: J. Appl. Phys. 136, 064501 (2024); doi: 10.1063/5.0215449

Submitted: 24 April 2024 · Accepted: 20 July 2024 ·

Published Online: 8 August 2024



Cheul Hyun Yoon,  Gyeong Min Seo,  Seok Hyun Yoon,  and Byoung Don Kong^{a)} 

AFFILIATIONS

Department of Electrical Engineering, Pohang University of Science and Technology (POSTECH), Pohang 37673, Republic of Korea

^{a)}Author to whom correspondence should be addressed: bdkong@postech.ac.kr

ABSTRACT

We investigate the potential of nanovacuum devices utilizing graphene edges as field emitters, with their work function modulated by a nearby gate on the graphene surface. Unlike metals, the semi-metallic nature of graphene enables modulation of the Fermi level and work function via the surface field. This modulation alters the potential barrier for field emission. Our simulation study reveals that device operation critically depends on two screening factors—horizontal and vertical. Horizontally, work function modulation occurs when the emitter edge is within the critical screening length from the gate edge. Vertically, the effectiveness of work function modulation diminishes beyond the second layer of multi-layer graphene due to surface field screening by the first layer. Our simulations demonstrate that maintaining the vacuum channel on tens of nanometer scale enables transistor-like operation of the device, with remarkably high cut-off frequencies and maximum oscillation frequencies ranging from 0.45 to 0.71 and 32.9 to 40.5 THz, respectively, under source–drain bias from 90 to 100 V.

© 2024 Author(s). All article content, except where otherwise noted, is licensed under a Creative Commons Attribution-NonCommercial-NoDerivs 4.0 International (CC BY-NC-ND) license (<https://creativecommons.org/licenses/by-nc-nd/4.0/>). <https://doi.org/10.1063/5.0215449>

I. INTRODUCTION

Graphene has attracted significant attention as a prospective field emission source in vacuum devices.^{1–8} Its atomistic thickness induces a substantial field enhancement effect at its edges, offering a unique property alongside reproducible performance due to its high stability.^{1–10} This characteristic envisions an unconventional atomistic scale emitter, a feat challenging to achieve with traditional emitters such as refractory metals (W, Mo, etc.) or semiconductors, given the difficulty in fabricating atomically thin or sharp emitters with these materials, not to mention concerns regarding resistance and stability. Adoption of a graphene emitter enables the realization of nanovacuum transistors (NVTs), leveraging the scattering-free transport of the vacuum channel and graphene's high carrier mobility. Particularly, NVTs and graphene channel-based field-effect transistors (FETs) emerge as promising candidates for high-frequency devices owing to high electron velocity.^{11–17}

Diverse investigations into graphene emitters have explored two primary arrangements: vertical and horizontal. In the vertical structure, graphene is positioned perpendicular to the substrate, while in the horizontal structure, the graphene emitter aligns parallel to the substrate.^{3–10} Several studies underscore the potential of

graphene emitter-based NVTs.^{1–8} Notably, the edge-to-edge structure has demonstrated field emission modulation and three-terminal operations by incorporating a gate between two graphene edges, separated by a few micrometers.⁴ Nevertheless, in all cases, field emission modulation occurs either through a single anode or another gate electrode situated between the emitter and the anode.^{14–16}

An unexplored opportunity lies in the distinctive semi-metallic nature of graphene. Unlike typical metals with a fixed work function, graphene's work function can be adjusted by the vertically applied electric field on its surface.^{18–20} The work function corresponds to the height of the potential barrier in field emission. Therefore, modulation of the work function can lead to modulation of field emission. However, this modulation typically occurs only beneath the surface where the vertical electric field is applied, usually beneath the gate. The influence of the vertical field diminishes within the screening length along the lateral direction. Consequently, if the emission edge is situated close to the gate within the screening length, the work function at the edge can be controlled via the gate on the surface, thereby modulating field emission.

20 September 2025 15:56:37

This study delves into the possibilities of modulating graphene edge field emission through a gate on the graphene surface. We developed a simulator for such systems that accurately considers graphene's massless Dirac fermions and examined the device performance under various bias conditions. The proposed structure unveils a unique potential for a high-power RF device, surpassing the operational performance of conventional solid-state devices. Additionally, we investigated structural requirements to maximize device performance, such as the relationship between the extended edge and the screening length, as well as the number of graphene layers.

II. VACUUM DEVICE MODELING

A. Theoretical background

Figure 1(a) depicts the schematic diagram of the studied structure. A protruded graphene edge (PGE) with a length of L_{PGE} functions as a field emitter (cathode), separated by vacuum from a drain (anode). Due to the similar configuration, scale, and function, naming conventions for the three terminals of FETs are used. A gate electrode, which modulates the emission current, is positioned before the PGE, vertically separated by dielectric, and the other side of graphene is connected to a source electrode. The Fermi energy level (ϵ_F) and the carrier density under the gate are modulated by the gate bias. Since the work function is the energy difference between ϵ_F and vacuum level, graphene's work function under the gate region can be controlled by the gate bias. Actually, the work function change is not limited to under the gate but extends to the nearby gate edge within the screening length. When PGE exists within this screening length, one can expect emission control by the gate bias.

The reasoning behind this structure is to confine all component arrangements into the nanoscale. In usual vacuum transistors, the gate is located between the anode and cathode, which always makes the vacuum channel include the gate length.²¹ In this case, as the channel length decreases, the gate length should also be shortened, while the shortened gate length can bring multiple issues such as increased resistance, not to mention the difficulties in the fabrication of such complex nanostructures. Additionally, the gate electrode is positioned completely out of sight in the emitted electrons' view, so the leakage current can be greatly suppressed. In conventional structures, the gate electrodes are placed between the emitter and drain. Naturally, some portions of electrons are attracted to gates. This can become severe, especially in nanovacuum devices.²¹

The unique single atom thick geometry of the graphene edge allows the nanoscale field emitter, as illustrated in Fig. 1(b). Due to the local field enhancement effect near the single-atom-thick edge, the probability of quantum tunneling of electrons at the emitter apex exponentially increases as the potential barrier thickness decreases by bending of the vacuum energy level. As a result, the emission current is indirectly modulated by altering the Fermi level of the graphene edge under the gate region by the Fowler–Nordheim (FN) theory. Thus, the device operates on completely distinct principles that differ from those of solid channel FETs. In MOSFETs, for instance, electrons are thermionically injected from the source into the channel, which is composed of a semiconductive medium, and then drift toward the drain. Contrary to this, in NVTs, electrons confined at the PGE tunnel through a triangular barrier quantum-mechanically to the vacuum channel (field emission). The emitted electrons accelerate by the applied electric field until they eventually arrive at the drain. While tunneling current may occur from the

20 September 2025 15:56:37

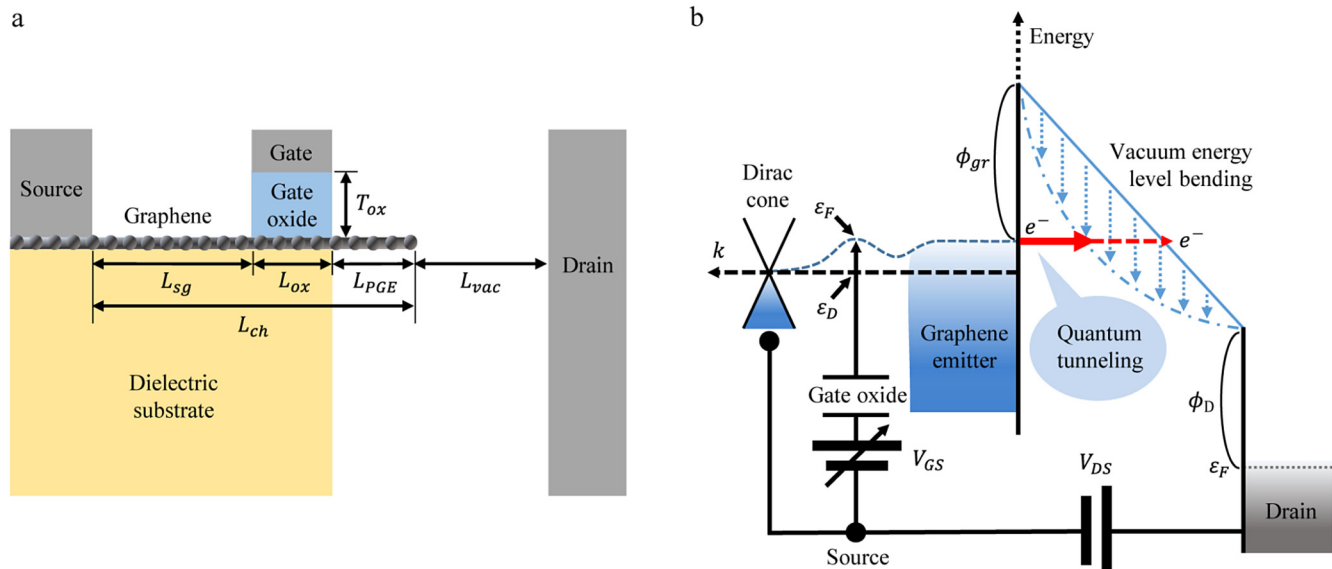


FIG. 1. (a) Schematic of the studied vacuum channel FET. Dimensions and parameters are summarized in Table 1. (b) Illustration of device operation. Gate potential variation of the metal–insulator–graphene structure induces the modulation of the Fermi level near the graphene edge.

gate electrode to the drain electrode as the length of the vacuum channel decreases, its quantity is significantly negligible compared to the overall tunneling current due to the large field enhancement factor at the PGE.

To describe the complex carrier dynamics, our simulation scheme divided the channel into two regions: graphene and vacuum. The two sets of equations governing each region's carrier dynamics were coupled with Poisson equations for field distribution, and the solutions for the nonlinear coupled equations were found by the iterative method.

1. Graphene region

The carrier dynamics within graphene can be described by the well-known linear energy-momentum dispersion relation

$$\varepsilon - \varepsilon_D = \pm \hbar v_F |\vec{k}|, \quad (1)$$

where ε represents the energy of carriers with the momentum state of wave vector \vec{k} in a two-dimensional plane ($|\vec{k}| = \sqrt{k_x^2 + k_y^2}$). ε_D is the Dirac point in the band diagram, commonly used as the reference point for carrier energy. \hbar is Planck's constant, and v_F is the Fermi velocity of carriers, approximately 10^6 m/s.²² The positive and negative signs in Eq. (1) correspond to the conduction and valence bands, respectively.

The density of states (DOS) in both bands has linear relations with energy, expressed as follows:

$$D_C(\varepsilon) = \frac{g_s g_v \varepsilon - \varepsilon_D}{2\pi (\hbar v_F)^2}, \quad (2a)$$

$$D_V(\varepsilon) = \frac{g_s g_v \varepsilon_D - \varepsilon}{2\pi (\hbar v_F)^2}, \quad (2b)$$

where g_s and g_v are the spin and valley degeneracies, respectively, both equal to two. The electron concentration (n) and the hole concentration (p) can be found as

$$n = \int_{\varepsilon_D}^{\infty} D_C(\varepsilon) f(\varepsilon) d\varepsilon = N_G \mathcal{F}_1(\eta_F), \quad (3a)$$

$$p = \int_{-\infty}^{\varepsilon_D} D_V(\varepsilon) [1 - f(\varepsilon)] d\varepsilon = N_G \mathcal{F}_1(-\eta_F), \quad (3b)$$

where $f(\varepsilon)$ is the Fermi-Dirac distribution, N_G is the effective graphene sheet density, and \mathcal{F}_1 is the complete Fermi-Dirac integral with index $i = 1$. N_G can be found as

$$N_G = \frac{g_s g_v}{2\pi} \left(\frac{k_B T}{\hbar v_F} \right)^2. \quad (4)$$

$\mathcal{F}_1(\pm \eta_F)$ is given by

$$\mathcal{F}_i(\pm \eta_F) = \frac{1}{\Gamma(i+1)} \int_0^{\infty} \frac{u^i}{1 + e^{\mp \eta_F} e^u} du, \quad (5)$$

where Γ is the gamma function and η_F is the normalized Fermi

energy level, ε_F , relative to ε_D such as

$$\eta_F = \frac{\varepsilon_F - \varepsilon_D}{k_B T}. \quad (6)$$

Here, k_B is Boltzmann's constant and T is the absolute temperature. In usual calculations for graphene FETs, the Fermi-Dirac distribution is approximated with the Maxwell-Boltzmann distribution, which can be justified with moderate carrier densities. However, the expected ε_F range is much broader, implying very high or low carrier densities where the approximation may be inappropriate. Thus, the Fermi-Dirac distribution function was used in all our calculations. Additionally, the current-voltage (I-V) characteristics of a graphene FET without the vacuum channel were calculated and compared with the experimental results as a sanity test. The developed simulator successfully regenerated the I-V relations from the literature.²²

2. Field emission and vacuum region

Charge transport through the vacuum channel is modeled using the continuity equation and the Fowler-Nordheim tunneling theory (or direct tunneling model of Simmons tunneling model with several energy levels) in a similar way to the literature.²³⁻²⁶ The Fowler-Nordheim (FN) equation correlates the current density (J) to various factors including the work function of the PGE (ϕ), the geometrical efficiency factor (η), the field enhancement factor (β), and the electric field (E) induced on the PGE. It is expressed as

$$J = \eta a \frac{(\beta E)^2}{\phi} \exp\left(-b \frac{\phi^{3/2}}{\beta E}\right). \quad (7)$$

Here, a and b represents constants ($a = 1.54143 \times 10^{-6}$ A eV/V², $b = 6.83089 \times 10^3$ V eV^{-3/2}/μm). Although η is assumed to be 1, the calculation of J takes into account the collective influence of neighboring meshes, ensuring full consideration of geometric variations. The determination of ϕ originates from the graphene region, while β and E are derived from the solution of the Poisson equation for discretized nodes surrounding the graphene edge, dynamically.

It is pertinent to note that the literature exhibits a wide range of values for β , spanning several thousand units.³ This variance arises due to β 's dependence on factors such as electrode configurations and bias conditions. Consequently, in our simulations, β is recalculated at each iterative step by evaluating the derivatives of electric potential distribution.

Two crucial points merit mention: First, the determination of J accounts for emission currents from all nodes, encompassing both surface and edge emissions. Second, we omit the consideration of Coulomb repulsion among emitted electrons, given the parallel distribution of electric field strength toward the drain and the nanoscale dimensions of the vacuum channel.

B. Numerical details

During the iterative routines, we determined the appropriate Fermi energy level relative to the Dirac point and computed the current densities for discretized nodes. This iterative process was also applied to the electric potentials in the vacuum region. The iterative procedure persisted until the system satisfied the required criteria for numerical convergence. The details of the simulated

TABLE I. Device parameters and dimensions used in this paper, unless otherwise noted.

Parameter (unit)	Value
L_{sg} (nm)	50
L_{ox} (nm)	15
L_{PGE} (nm)	5–35
L_{ch} (nm)	70–100
L_{vac} (nm)	25, 50, 75
T_{ox} (nm)	15
ϵ_{vac} (F/m)	$8.854\,188 \times 10^{-12}$
$\epsilon_{Si_3N_4}$ ²⁷	7
$\epsilon_{Al_2O_3}$ ²⁷	10
$\phi_{Pd} (= \phi_D)$ (eV) ²⁸	5.22
$\chi_{graphene}$ (eV)	4.56
μ_n (cm ² /V s)	5000
μ_p (cm ² /V s)	5000
v_F (m/s)	10^6

device structures and parameters are summarized in Table I. Apart from the graphene emitter, the substrate and gate oxide were assumed to be silicon nitride (Si_3N_4) and aluminum oxide (Al_2O_3), respectively. Oxide length (L_{ox}) and thickness (T_{ox}) were set to be 15 nm. For the metal electrodes (source, drain, and gate), palladium with a work function of 5.22 eV was utilized.²⁸ Two types of graphene emitters, monolayer and bilayer, were examined. One end of graphene formed a Schottky contact with the source electrode, while the other edge formed PGEs with various lengths (L_{PGE}). Specifically, L_{PGE} ranging from 5 to 35 nm was studied to assess the effect of the screening lengths. Considering the thickness of graphene, the vertical lattice spacing of 3.45 Å for graphene layers was used. The vacuum channel length (L_{vac}), defined as the straight-line distance from the graphene edge to the drain area, was varied from 25 to 75 nm. For all simulations, a room temperature of 300 K was assumed.

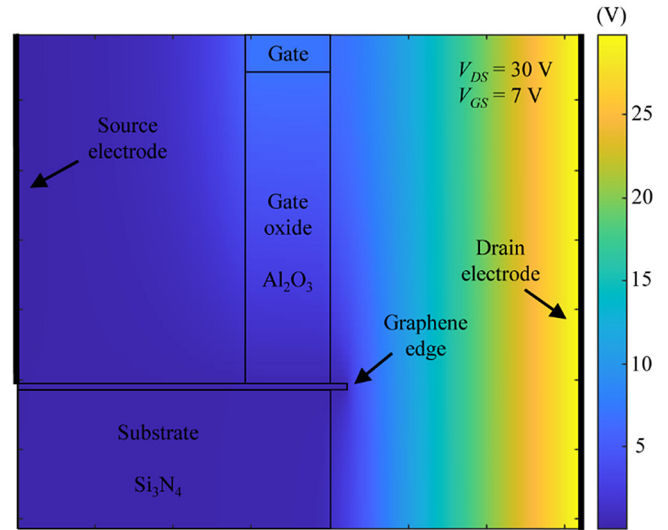
As shown in Fig. 2, device operation was successfully simulated using the specified physical model and parameters. The electric potential in each region of the device was accurately calculated, revealing the expected features under the given bias condition. Notably, the high conductivity of graphene results in the accumulation of negative charges at the emission tip induced by drain voltage. The field enhancement effect at the graphene edge produces a rapid potential variation in the vacuum channel near the emitter. Interestingly, the impact of gate bias modulation on this potential distribution, particularly along the vacuum channel near the PGE, is minimal. This indicates that the modulation of the emission current is due to work function changes rather than potential changes in the vacuum channel caused by gate bias variation.

III. RESULTS

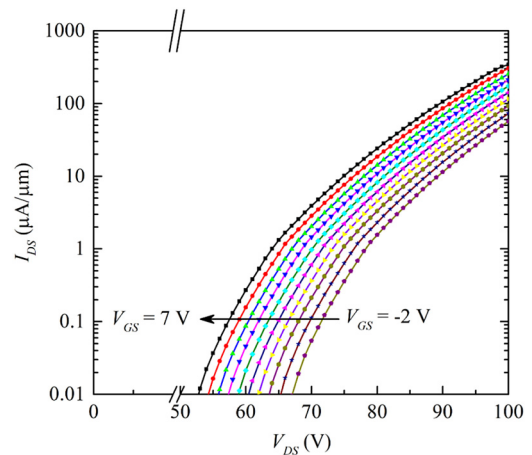
A. Monolayer graphene emitter

1. Emission current modulation and electronic properties

The simulation results clearly demonstrate the feasibility of modulating the field emission current through work function

**FIG. 2.** Electric potential distribution of the system. The effect of gate biasing is visualized through the variation in electric potential. The scale has been exaggerated in the vertical direction to enhance visual understanding of the device structure. The electric potential changes in parallel to the surface of the drain electrode, indicating that emitted electrons are not expected to leak to the gate electrode.

control. As depicted in Fig. 3, with $L_{PGE} = 5$ nm, an increase in tunneling current due to variations in V_{GS} was observed. The emission current exhibits an exponential increase with the rise in V_{DS} , indicative of the typical characteristics of quantum tunneling. These findings underscore the effectiveness of the proposed approach in on/off switching and current modulation. Notably, a gradual shift

**FIG. 3.** I_{DS} - V_{DS} characteristics as a function of gate bias ($V_{GS} = -2 \sim 7$ V with a 1 V step). The emission current exhibits an exponential increase with the rise in source-drain bias (V_{DS}), while the modulation of the emission current is confirmed with the changes in gate bias.

20 September 2025 15:56:37

in calculated threshold voltages (V_{th}), denoting the minimum voltage requisite at the gate terminal of a transistor to enable significant current flow between the source and drain, was observed as V_{GS} increased from $V_{GS} = -2$ to 7 V. Specifically, V_{th} was measured at 52 and 66 V at $V_{GS} = -2$ and 7 V, respectively. The derivative of V_{th} with respect to V_{GS} displayed a variation, which is attributed to the DOS of the graphene emitter.

Figures 4(a) and 4(b) illustrate ϵ_F , ϵ_D , and $\epsilon_F - \epsilon_D$ along graphene at two different gate biases. As the charge density of graphene is tied to $\epsilon_F - \epsilon_D$, ϵ_F and the work function of the PGE are influenced by two electrodes—the drain and gate. Under the influence of the electric field from the drain, graphene is capacitively charged with n , and $\epsilon_F - \epsilon_D$ is progressively increased along the channel. At the PGE tip, ϵ_F and $\epsilon_F - \epsilon_D$ reach their maximum, leading to a reduction in the work function and easier emission of electrons to the vacuum. In this state, gate bias also significantly influences ϵ_F and $\epsilon_F - \epsilon_D$ under and near the gate. Carrier concentration significantly increases beneath gate oxide, where the gate bias directly controls the Fermi level of the graphene channel. The changes in ϵ_F and $\epsilon_F - \epsilon_D$ (from 1.66 to 1.75 eV at the edge) when V_{GS} is increased from 0 to 7 V are distinctively noticeable from Fig. 4(b). While the carrier concentration undergoes a rapid change away from the edge of the gate, the influence of the gate bias penetrates through the PGE. As such, the surface field induced by the gate bias modulates the emission current by directly altering the work function.

2. Work function controllability and screening length

The PGE length (L_{PGE}) is a critical factor determining the device's performance as it significantly influences the potential distribution near the emitter tip, thereby affecting the level of field enhancement effects and FN tunneling. Figure 5 summarizes the variations of work function with respect to V_{GS} modulation as a function of L_{PGE} for two different V_{DS} conditions. The modulated amount of work function ($\Delta\phi_{gr}$) when V_{GS} is modulated from 0 to 7 V decreases as L_{PGE} increases. Simultaneously, a smaller $\Delta\phi_{gr}$ is observed for a larger V_{DS} . Specifically, $\Delta\phi_{gr}$ is reduced from 0.51 to 0.094 eV as V_{DS} is increased from 1 to 100 V with $L_{PGE} = 5$ nm.

The sensitivity, $\Delta\phi_{gr}/\Delta V_{GS}$, relies mainly on two factors. One is the screening by mobile charges within the graphene channel, and the other is the energy-dependent DOS of graphene. In graphene, the DOS has a linear dependence on $\epsilon - \epsilon_D$ unlike a 3D bulk material whose dependence is $\sqrt{\epsilon}$, and the increase in carrier density becomes rapid when ϵ_F deviates further from ϵ_D . At higher V_{DS} , a substantial current flows through the graphene channel, and almost the entire graphene region becomes negatively charged. As a result, the intense screening effect reduces the influence of the gate bias on the PGE tip significantly. Simultaneously, the responsiveness to gate bias modulation becomes relatively diminished due to the large DOS. These two factors collectively reduce the controllability of the work function by the gate bias.

The trend observed in Fig. 5 generally holds under different V_{GS} conditions. However, slight variations in the trend may occur if, during gate bias modulation, ϵ_F crosses ϵ_D within the PGE. For instance, due to graphene's unique properties, regions of negative transconductance can arise during V_{GS} modulation. If the gate bias is exclusively varied within this region, the work function change at

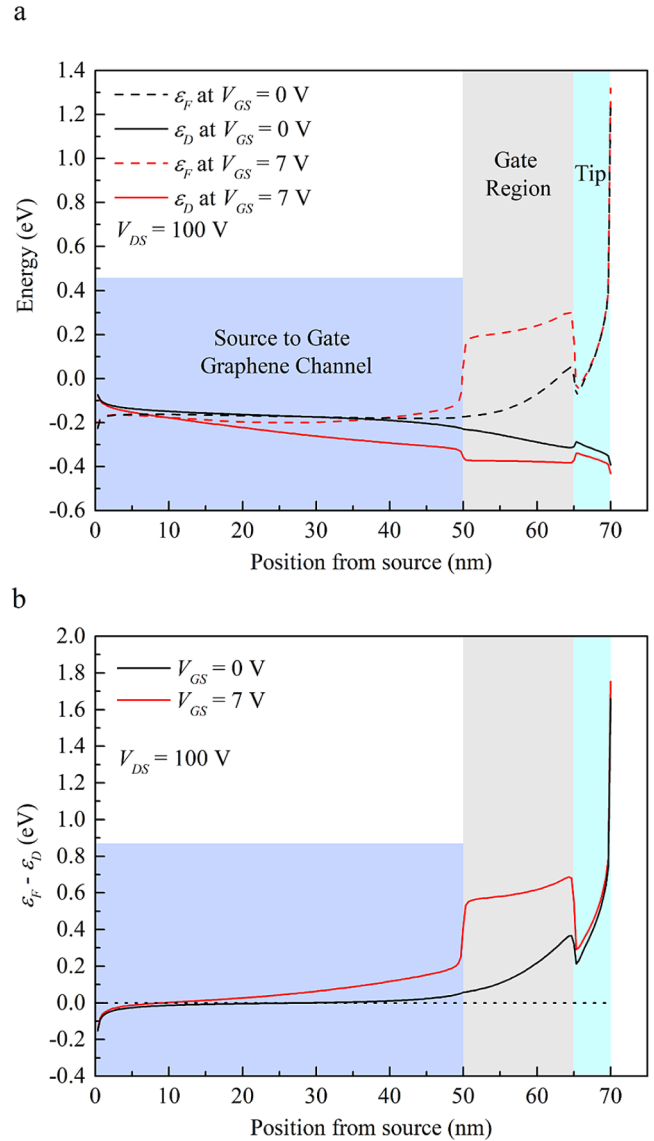


FIG. 4. Band diagram and $\epsilon_F - \epsilon_D$ along the graphene channel from source-graphene contact to PGE under $V_{DS} = 100$ V, and $V_{GS} = 0$ (black) and 7 (red) V, respectively. (a) ϵ_F and ϵ_D are notably influenced by the surface field induced by gate bias. (b) The concentration of charge carriers traversing the graphene channel is modulated by the gate voltage-induced work function modulation. $\epsilon_F - \epsilon_D$ at PGE area (light blue) varies as the gate bias changes. At the source-graphene contact, the Fermi level is lower than the Dirac point due to the pinning effect induced by the Schottky junction with the source electrode.

the graphene edge may become negative. Nonetheless, in most cases, the trend observed in Fig. 5 remains prevalent.

Consequently, in general, under high V_{DS} conditions, a shorter L_{PGE} is required for the operation, considering the high-concentration of mobile charges within the protrusion region. However, L_{PGE} is also associated with the field enhancement effect,

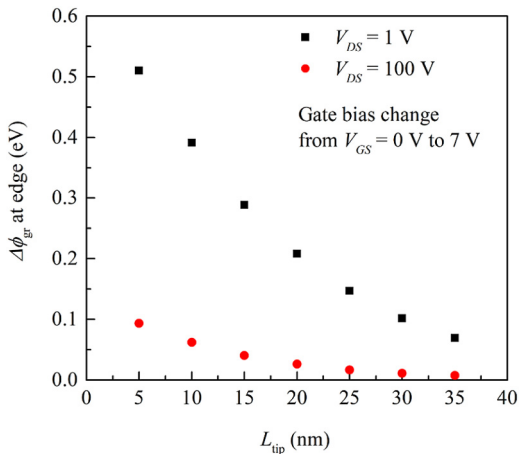


FIG. 5. Change in work function ($\Delta\phi_{gr}$) at the PGE edge as a function of the PGE length (L_{PGE}). The screening effect reduces $\Delta\phi_{gr}$ as L_{PGE} increases, significantly influencing the devices' operation. While the modulation of the emission current is primarily governed by L_{PGE} , the controllability of the work function also relies on the quantum capacitance of the graphene channel, which varies with changes in external bias conditions.

and a shorter L_{PGE} may weaken the concentrated electric field due to the larger influence from the nearby dielectric, leading to a substantial reduction in emission current. Therefore, designing an appropriate emitter length that balances work function controllability and emission current becomes crucial.

Since the electric field that induces FN tunneling is crucial to the emission current, it also depends on the length of the vacuum channel (L_{vac}) for the same applied V_{DS} . As shown in Fig. 6, a reduction in the vacuum channel length results in an exponential increase in emission current. This is because the electric field is stronger, and the equipotential lines around the tip become denser.

B. Bilayer graphene emitter

A device with a bilayer graphene emitter was simulated by inserting an additional graphene layer. For the two graphene layers, all structural parameters were maintained the same. For multilayer graphene, it is known that its unique two-dimensional structure suppresses interlayer conductivity, resulting in significant interlayer screening.²⁹ This vertical (to the substrate) screening markedly impacts device operation, in contrast to the monolayer graphene emitter.

Intriguingly, the emission current with the bilayer graphene emitter significantly decreases compared to the monolayer counterpart, as shown in Fig. 7. It appears that a substantial difference in the emission current exists between the 1st layer (graphene contacting gate oxide) and the 2nd layer (graphene contacting the substrate), and the emission currents from the two graphene edges do not simply add up. Additionally, there was a difference in the threshold voltages between the two layers. For instance, at $V_{GS} = 0$ V, the threshold voltage for the 1st layer was 13 V, whereas

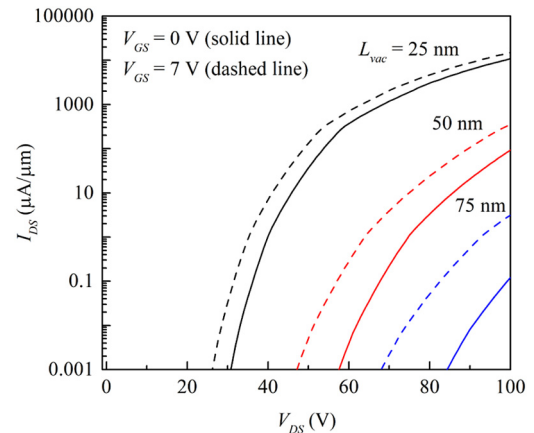


FIG. 6. I_{DS} - V_{DS} characteristics with variation of the vacuum channel length. Black, red, and blue lines correspond to the cases where L_{vac} is 25, 50, and 75 nm, respectively. As the length of the vacuum channel decreases, there is an exponential increase in the emission current. The reduction in the vacuum channel length leads to a significant augmentation of the electric field at the PGE edge, inducing strong vacuum energy level bending in the vacuum channel and, consequently, causing a sharp escalation in the probability of quantum tunneling.

it was 58 V for the 2nd layer. When $V_{GS} = 7$ V, these values shifted to 8 and 51 V, respectively.

The significant reduction in emission current in the bilayer emitter stems from the charge dispersion between the two layers for V_{DS} . The charge induced by V_{DS} at the emitter tips is distributed across both layers, resulting in a smaller amount of charge in each layer compared to the monolayer. In graphene, this means $\mathcal{E}_F - \mathcal{E}_D$ is smaller, and the work function at the emitter tip is larger. Since the emission current has an exponential dependence on the barrier height, which is the work function, the bilayer graphene emitter shows a substantially lower emission current for the same V_{DS} .

Additionally, the bilayer emitter exhibits distinct responses to gate bias. This discrepancy arises due to a screening effect present in multilayer graphene against out-of-plane electric fields. As depicted in Figs. 8(a) and 8(b), the \mathcal{E}_F of the 1st layer exhibits a more pronounced response to V_{GS} , whereas the effect is markedly attenuated in the 2nd layer. A substantial portion of the surface field applied to the 1st layer is screened by inducing charge in this layer, thereby diminishing the influence of V_{GS} on the 2nd layer. This vertical screening exerts a significant impact on the modulation of the work function of the PGE tip, consequently leading to a drastic reduction in the controllability of PGE's work function by the gate.

The reduction in controllability due to vertical screening should impact device performance, even as the number of layers increases beyond bilayer graphene. The influence of vertical screening in multilayer graphene FETs has been studied, as noted in Ref. 29. Since the proposed device relies on direct work function modulation through the vertically applied surface field from the gate, this issue inevitably arises in a single-gate structure. However, in a double-gate structure where the surface field is applied by both top and bottom gates, these effects can be alleviated to some extent.

20 September 2025 15:56:37

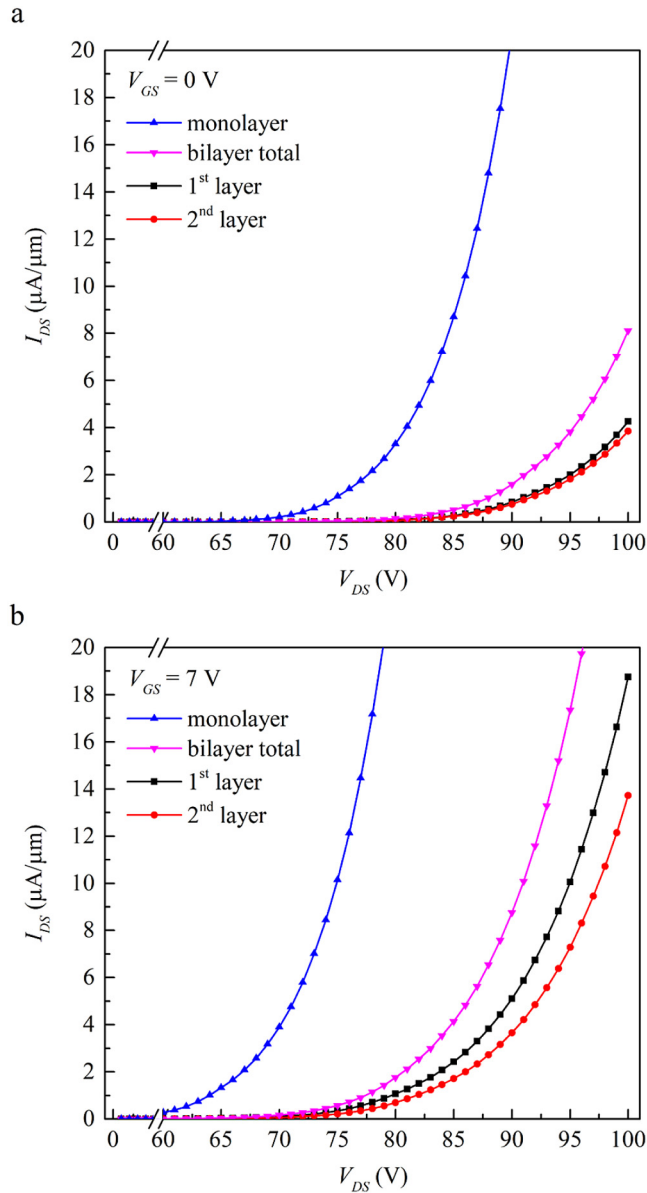


FIG. 7. I - V curves of the bilayer graphene emitter compared to the monolayer graphene emitter. (a) $V_{GS} = 0$ V and (b) $V_{GS} = 7$ V. The vertical screening effect between two graphene layers substantially affects device performance. The decrease in the quantum capacitances in each layer and the lateral screening length result in a decreased emission current.

C. Transistor performance and frequency response

1. Transconductance

Figure 9(a) illustrates the transconductance (g_m) of devices featuring a 50 nm vacuum channel, comparing monolayer and bilayer graphene emitters. g_m was determined by numerically

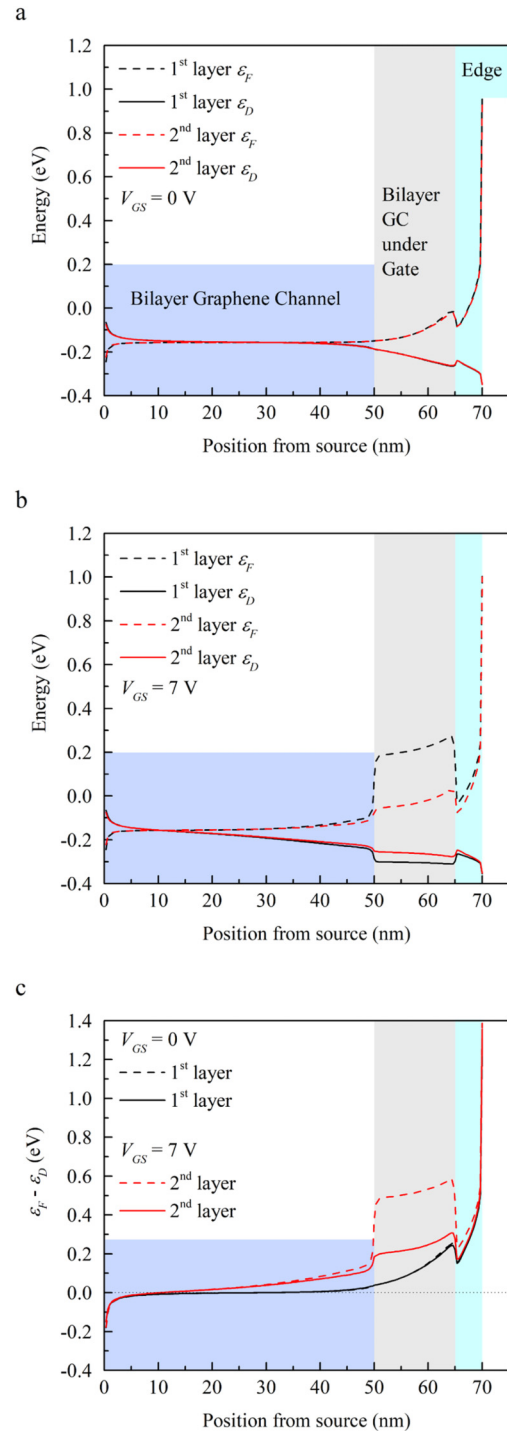


FIG. 8. Band diagrams of the bilayer graphene emitter along the graphene channel. (a) $V_{GS} = 0$ V and (b) $V_{GS} = 7$ V. As V_{GS} increases, the charge concentration in the 1st layer substantially increases, which screens the surface field applied to the 2nd layer. As a result, the work function controllability is significantly suppressed.

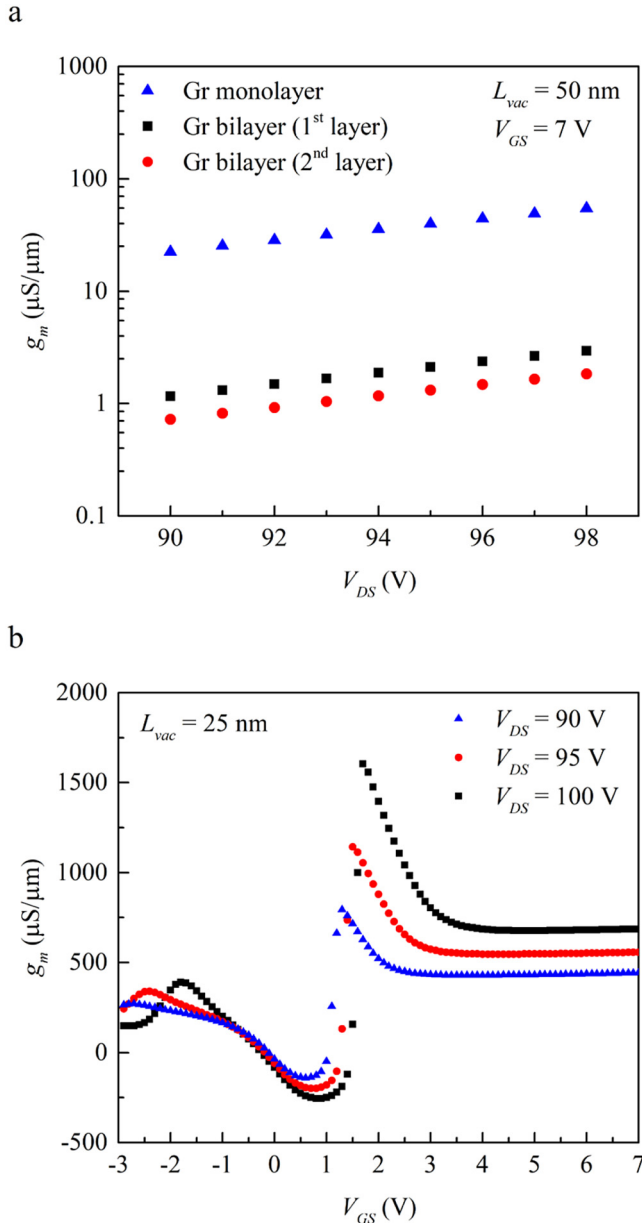


FIG. 9. (a) Comparison of transconductance (g_m) between monolayer and bilayer graphene emitters. (b) Transconductance of the monolayer graphene emitter with a 25 nm vacuum channel for three different drain biases: $V_{DS} = 90$, 95, and 100 V.

estimating $\Delta I_{DS}/\Delta V_{GS}$. Under identical device structures and bias conditions, the monolayer emitter exhibits a significantly higher g_m compared to the bilayer emitter, attributed to various screening effects present in the bilayer configuration.

Figure 9(b) depicts the g_m of a monolayer emitter device with a reduced vacuum channel length (25 nm), aimed at improving g_m

under the same ΔV_{GS} . When V_{GS} is varied for a fixed V_{DS} , g_m exhibits a similar trend to graphene FETs.^{30,31} g_m undergoes a sharp transition around $\epsilon_F \sim \epsilon_D$, where the polarity of graphene changes from p- to n-type. As V_{DS} increases, the transition point shifts toward higher values, attributed to the shift in ϵ_F within the graphene channel. At $V_{DS} = 90$ V, g_m reaches its maximum value of $792.5 \mu\text{S}/\mu\text{m}$; at 95 V, $1142.2 \mu\text{S}/\mu\text{m}$; and at 100 V, $1604.1 \mu\text{S}/\mu\text{m}$, which is 1.34–1.96 times larger than the typical g_m value of GaN HEMT.³²

It is worth mentioning the feasibility of applying 100 V across a 25 nm vacuum gap. This pertains to the issue of how much field is applied on the insulating dielectric rather than the vacuum gap itself. For instance, the breakdown electric field of a conventional dielectric such as Si_3N_4 is about ~ 11 MV/cm.³³ To support 100 V, more than 91 nm of Si_3N_4 length is required. Creating a 50 nm deep trench on the Si_3N_4 substrate would extend the physical distance between the electrodes where the bias is applied, providing the necessary separation to apply the desired potential. Since realizing a few μm deep trench by reactive ion etching is routinely performed in modern semiconductor fabrications, the device structure is an achievable goal, and even further enhancement is possible.

2. RF performances

Frequency characteristics were estimated using the small-signal equivalent circuit model.⁴ The circuit model is depicted in Fig. 10, where the cut-off frequency (f_T) is given by

$$f_T = \frac{g_m}{2\pi(C_T + C_{GD})}. \quad (8)$$

Here, C_T is the capacitive component seen to the gate electrode, comprising the gate dielectric capacitance (C_{ox}) and the quantum capacitance (C_Q) of the graphene channel. Specifically, C_T is given as $C_T = 1/(1/C_{ox} + 1/C_Q)$, where $C_{ox} = \epsilon_{ox}/t_{ox}$ and C_Q is $C_Q[\mathcal{F}_0(\eta_F) + \mathcal{F}_0(-\eta_F)]$, with $C_q = q^2 N_G/k_B T$.^{22,34,35}

The estimated f_T , as illustrated in Fig. 11(a), exhibits variations according to the bias conditions. For a fixed V_{DS} , f_T shows a maximum when ϵ_F is close to ϵ_D , where a sharp transition occurs and saturates for larger V_{GS} . For instance, at

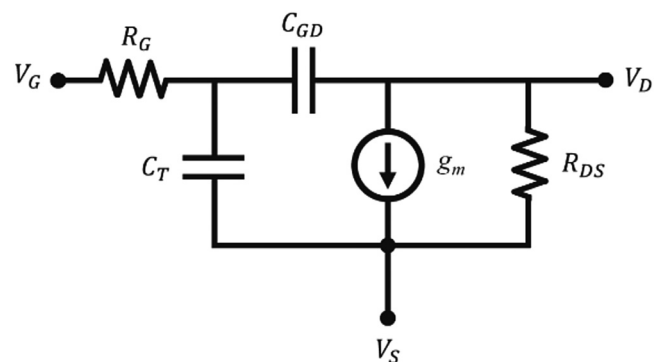


FIG. 10. Equivalent circuit for frequency analysis. C_T is the total gate capacitance, which includes gate oxide capacitance and quantum capacitance.

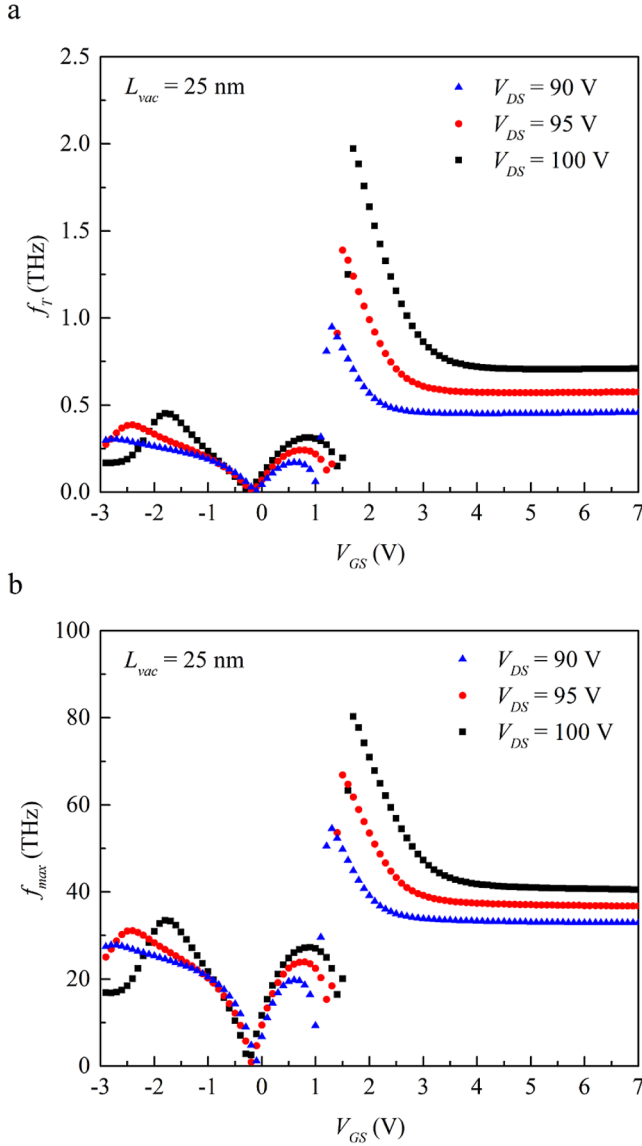


FIG. 11. (a) Cut-off frequency (f_T) and (b) Maximum-oscillation frequency (f_{max}). V_{GS} ranges from -3 to 7 V with three different drain bias conditions: $V_{DS} = 90, 95$, and 100 V.

$V_{DS} = 100$ V, the maximum f_T was 1.97 THz, and the saturated f_T at higher V_{GS} was 0.71 THz. Before ε_F crosses ε_D , which corresponds to a lower or negative V_{GS} , f_T values range from 0.16 to 0.45 THz. It should be noted that there is a region of negative g_m , typically located between $V_{GS} = 0$ and 1 V. This is where the transition from n- to p- type occurs, and in such cases, the emission current decreases as V_{GS} increases. For this region, absolute values of g_m were used to estimate f_T since they are related to the frequency response.

The maximum-oscillation frequency (f_{max}) was calculated as

$$f_{max} = \frac{g_m}{2\pi C_T} \frac{1}{\sqrt{(R_G/R_{DS}) + g_m R_G (C_{GD}/C_T)}}, \quad (9)$$

which represents the frequency of unity unilateral power gain. R_G was set to be 1.4×10^{-3} , deduced from a similar size of gate electrode, whereas R_{DS} was set to be about a value of a few ohm scales, estimated from the simulation. As shown in Fig. 11(b), the as-calculated f_{max} is in the tens of the THz scale. For example, at $V_{DS} = 100$ V, f_{max} increases up to 80.3 THz at the maximum and gradually saturates to 40.5 THz.

The exceptional f_T and f_{max} are primarily attributed to the small C_{GD} , large R_{DS} , and substantial g_m . C_{GD} is determined by the structure of the device, whereas R_{DS} and g_m are influenced by the fundamental characteristics of the studied device. Notably, R_{DS} relies on the unique feature of the vacuum channel, which does not impede carrier mobility. The vacuum channel, devoid of scattering other than electron-electron scattering, ensures rapid frequency response due to the swift movement of carriers. However, the resistance component in the equivalent circuit is significant due to the nature of the emission current, which depends on the quantum tunneling probability. Additionally, high transconductance is determined by various components such as the energy-DOS relationship of the graphene emitter and the complex dynamics between quantum tunneling probability and PGE's work function. Particularly, the property of gate oxide and the gate structure can significantly affect the transconductance, which, in turn, can alter the device's frequency characteristics, threshold voltage, and breakdown voltage, thereby substantially changing the device's operational characteristics. Consequently, these characteristics enable the operation of the device proposed in this study under high-frequency conditions. To push up the operation frequency of the studied device as high as possible, optimizing parameters such as L_{PGE} and L_{vac} , and the efficient design of the gate structure and materials are critical.

IV. SUMMARY AND CONCLUSIONS

In this paper, we introduce a novel approach for controlling field emission in a microscale vacuum channel transistor with a graphene edge emitter. By employing coupled equations for field emission to the vacuum and Dirac particles in the graphene channel, we assess the I-V characteristics and RF performance of the device. Our findings demonstrate transistor operation at a superior level compared to conventional solid-state devices. Notably, the estimated f_{max} reaches up to several tens of THz, driven by the vacuum separation between the output (drain) and the input (gate), thus offering a compelling alternative for realizing high-speed RF devices.

Our investigation unveils the pivotal role of screening effects along both horizontal graphene channels and vertical layers in optimizing device performance. Horizontally, the length of the protruded graphene edge (PGE) must be maintained within the screening length, which is contingent upon drain and gate bias. Vertically, monolayer graphene emerges as the optimal choice, as field enhancement and work function modulation drastically

diminish from the second layer onward due to screening by the top layer.

Contrary to expectations, the total current level of a bilayer emitter is smaller than that of a monolayer emitter, attributed to the distribution (or screening) of the field from the drain and gate. Additionally, our proposed modulation scheme offers the advantage of minimizing the vacuum channel length, aligning the operation voltage of the vacuum device with that of solid-state devices. Ultimately, our study charts a path toward compact micro-vacuum devices capable of operating beyond the limitations of conventional solid-state devices.

ACKNOWLEDGMENTS

This work was supported by “Samsung Research Funding and Incubation Center” of Samsung Electronics (No. SRFC-IT2102-01) and the National Institute of Information and Communication Planning and Evaluation (No. 2022-0-00720) of Ministry of Science and ICT (MOTIE).

AUTHOR DECLARATIONS

Conflict of Interest

The authors have no conflicts to disclose.

Author Contributions

Cheul Hyun Yoon: Conceptualization (supporting); Data curation (lead); Formal analysis (equal); Funding acquisition (supporting); Investigation (equal); Methodology (supporting); Project administration (lead); Resources (lead); Software (lead); Supervision (lead); Validation (equal); Visualization (lead); Writing – original draft (lead); Writing – review & editing (lead). **Gyeong Min Seo:** Conceptualization (supporting); Data curation (supporting); Formal analysis (supporting); Funding acquisition (supporting); Investigation (supporting); Methodology (supporting); Software (supporting); Validation (supporting); Visualization (supporting); Writing – original draft (supporting); Writing – review & editing (supporting). **Seok Hyun Yoon:** Data curation (supporting); Formal analysis (supporting); Investigation (supporting); Methodology (supporting); Software (supporting); Validation (supporting); Visualization (supporting); Writing – review & editing (supporting). **Byoung Don Kong:** Conceptualization (lead); Data curation (supporting); Formal analysis (equal); Funding acquisition (lead); Investigation (equal); Methodology (lead); Project administration (lead); Resources (lead); Software (supporting); Supervision (lead); Validation (equal); Visualization (supporting); Writing – review & editing (lead).

DATA AVAILABILITY

The data that support the findings of this study are available from the corresponding author upon reasonable request.

REFERENCES

¹W. Zheng, X. Zhao, and W. Fu, *ACS Appl. Mater. Interfaces* **13**(8), 9561 (2021).

- ²Z.-S. Wu, S. Pei, W. Ren, D. Tang, L. Gao, B. Liu, F. Li, C. Liu, and H.-M. Cheng, *Adv. Mater.* **21**(17), 1756 (2009).
- ³L. Chen, H. Yu, J. Zhong, L. Song, J. Wu, and W. Su, *Mater. Sci. Eng. B* **220**, 44 (2017).
- ⁴J. L. Shaw, J. B. Boos, B. D. Kong, J. T. Robinson, and G. G. Jernigan, *J. Appl. Phys.* **125**(5), 054502 (2019).
- ⁵L. Chen, H. Yu, J. Zhong, C. Wu, L. Hu, and T. Zhang, *IEEE Trans. Electron Devices* **62**(12), 4305 (2015).
- ⁶Z. Xiao, J. She, S. Deng, Z. Tang, Z. Li, J. Lu, and N. Xu, *ACS Nano* **4**(11), 6332 (2010).
- ⁷S. Santandrea, F. Giubileo, V. Grossi, S. Santucci, M. Passacantando, T. Schroeder, G. Lupina, and A. Di Bartolomeo, *Appl. Phys. Lett.* **98**(16), 163109 (2011).
- ⁸H. Yamaguchi, K. Murakami, G. Eda, T. Fujita, P. Guan, W. Wang, C. Gong, J. Boisse, S. Miller, and M. Acik, *ACS Nano* **5**(6), 4945 (2011).
- ⁹M. Qian, T. Feng, H. Ding, L. Lin, H. Li, Y. Chen, and Z. Sun, *Nanotechnology* **20**(42), 425702 (2009).
- ¹⁰O. Girit, J. C. Meyer, R. Erni, M. D. Rossell, C. Kisielowski, L. Yang, C.-H. Park, M. Crommie, M. L. Cohen, and S. G. Louie, *Science* **323**(5922), 1705 (2009).
- ¹¹Y. Wu, K. A. Jenkins, A. Valdes-Garcia, D. B. Farmer, Y. Zhu, A. A. Bol, C. Dimitrakopoulos, W. Zhu, F. Xia, and P. Avouris, *Nano Lett.* **12**(6), 3062 (2012).
- ¹²Y. Wu, Y.-m. Lin, A. A. Bol, K. A. Jenkins, F. Xia, D. B. Farmer, Y. Zhu, and P. Avouris, *Nature* **472**(7341), 74 (2011).
- ¹³G.-J. Han, K. A. Jenkins, A. Valdes Garcia, A. D. Franklin, A. A. Bol, and W. Haensch, *Nano Lett.* **11**(9), 3690 (2011).
- ¹⁴J.-W. Han, D.-I. Moon, and M. Meyyappan, *Nano Lett.* **17**(4), 2146 (2017).
- ¹⁵J.-W. Han, J. Sub Oh, and M. Meyyappan, *Appl. Phys. Lett.* **100**(21), 213505 (2012).
- ¹⁶J.-W. Han, M.-L. Seol, D.-I. Moon, G. Hunter, and M. Meyyappan, *Nat. Electron.* **2**(9), 405 (2019).
- ¹⁷S. Srisophonphan, Y. S. Jung, and H. K. Kim, *Nat. Nanotechnol.* **7**(8), 504 (2012).
- ¹⁸J.-H. Huang, J.-H. Fang, C.-C. Liu, and C.-W. Chu, *ACS Nano* **5**(8), 6262 (2011).
- ¹⁹Y.-J. Yu, Y. Zhao, S. Ryu, L. E. Brus, K. S. Kim, and P. Kim, *Nano Lett.* **9**(10), 3430 (2009).
- ²⁰S. Naghdi, G. Sanchez-Arriaga, and K. Y. Rhee, *J. Alloys Compd.* **805**, 1117 (2019).
- ²¹J. Kim, J. Kim, H. Oh, M. Meyyappan, J.-W. Han, and J.-S. Lee, *J. Vac. Sci. Technol. B* **34**(4), 042201 (2016).
- ²²J. G. Champlain, *J. Appl. Phys.* **109**(8), 084515 (2011).
- ²³Y. Ang, S.-J. Liang, and L. Ang, *MRS Bull.* **42**(7), 505 (2017).
- ²⁴K. L. Jensen, *J. Vac. Sci. Technol. B* **21**(4), 1528 (2003).
- ²⁵J. G. Simmons, *J. Appl. Phys.* **34**(6), 1793 (1963).
- ²⁶R. H. Fowler and L. Nordheim, *Proc. R. Soc. Lond. Ser. A* **119**(781), 173 (1928).
- ²⁷J. Robertson, *Eur. Phys. J. Appl. Phys.* **28**(3), 265 (2004).
- ²⁸G. N. Derry, M. E. Kern, and E. H. Worth, *J. Vac. Sci. Technol. A* **33**(6), 060801 (2015).
- ²⁹M. A. Kuroda, J. Tersoff, and G. J. Martyna, *Phys. Rev. Lett.* **106**(11), 116804 (2011).
- ³⁰H. Xu, Z. Zhang, H. Xu, Z. Wang, S. Wang, and L.-M. Peng, *ACS Nano* **5**(6), 5031 (2011).
- ³¹B.-W. Hwang, H.-I. Yeom, D. Kim, C.-K. Kim, D. Lee, and Y.-K. Choi, *Solid State Electron.* **141**, 65 (2018).
- ³²N. C. Miller, A. Arias-Purdue, E. Arkun, D. Brown, J. F. Buckwalter, R. L. Coffie, A. Corrion, D. J. Denninghoff, M. Elliott, and D. Fanning, *IEEE J. Microw.* **3**(4), 1134 (2023).
- ³³C. Ng, K. Chew, and S. Chu, *IEEE Electron Device Lett.* **24**(8), 506 (2003).
- ³⁴T. Fang, A. Konar, H. Xing, and D. Jena, *Appl. Phys. Lett.* **91**(9), 092109 (2007).
- ³⁵J. Xia, F. Chen, J. Li, and N. Tao, *Nat. Nanotechnol.* **4**(8), 505 (2009).